Journal of Materials Chemistry A

ROYAL SOCIETY OF CHEMISTRY

PAPER

View Article Online
View Journal

Cite this: DOI: 10.1039/d6ta01009a

Magnetic nanoparticle constructs for *in situ* repair of critical cementitious infrastructure

E. Calì,*[ab] M. Pedrotti,*[c] G. Sernicola,[a] S. Fearn,[a] L. Vandeperre,[a] R. J. Lunn[c] and M. P. Ryan[ad]

Cement barriers in critical infrastructures, such as nuclear waste containment, can degrade and crack over time, enabling radionuclide release and further failure mechanisms. Repair in such hazardous scenarios is challenging, creating demand for remotely applicable solutions. This paper investigates silica-coated magnetic nanoparticles (SiO_2@Fe_3O_4 NPs) as a novel gelling material for sealing microcracks in cement. The nanofiller is developed by coating magnetic nanoparticles with a silica shell using the water-in-oil emulsion method. The magnetic core enables targeted emplacement of the NPs within cracks, whereas the silica shell undergoes gelling through siloxane network formation upon destabilization. The developed SiO_2@Fe_3O_4 NPs constructs exhibit high stability due to surface charge repulsion. Application of a 0.48 T magnetic field locally concentrate the NPs, overcoming electrostatic stabilization and inducing coalescence and subsequent gelling. This allows for the development of a magnetically drivable filler, that can be concentrated at the defect location and subsequently gelled. X-ray computed tomography (X-ray CT) and time-of-flight secondary ion mass spectrometry (ToF-SIMS) demonstrated the effectiveness of this process in filling artificial crack geometries, providing insights into the 3D spatial and temporal evolution of the repair. Moreover, Scanning Electron Microscopy combined with Energy Dispersive X-ray Spectroscopy analysis provided evidence of additional calcium–silicate–hydrate formation resulting from the reaction of the nanofiller with cations present in the cement. These results show for the first time that magnetic concentration can overcome charge-based stabilization of SiO_2@Fe_3O_4 NPs nanoparticles, enabling their use as highly effective material for sealing nano- and micro-cracks in physical barriers.

Received 2nd February 2026
Accepted 13th April 2026

DOI: 10.1039/d6ta01009a

rsc.li/materials-a

1 Introduction

Cementitious materials are widely used in critical infrastructure, but are susceptible to severe degradation phenomena, including cracking and spallation. In the nuclear industry, their potential as physical barriers for radionuclide containment in deteriorating nuclear infrastructure has been widely investigated.[1,2] Colloidal silica injected as a suspension of silica nanoparticles (NPs), has gained extensive interest in grout cracks in ageing UK waste vessels and limiting radionuclide migration into groundwater.[3–7] thanks to its low viscosity and its nanometre-scale particles. The sole use of SiO_2 as filling material bears, however, certain limitations,[4,8] as emplacement requires large hydraulic gradients, high-pressure injection is difficult to localize and can enlarge existing defects, thereby increasing leakage rates and the potential for contaminant migration and surrounding-material damage. Additionally, an accelerant (generally an electrolyte suspension) to destabilise the suspension of negative SiO_2 NPs and allow the creation of surface Si–O–Si (siloxane) bonds, *i.e.* formation of a hydrogel[9,10] must be used, posing a treat for chemical alteration of the system and the case for local cation leaching at the cement surface.[11]

Technologies using magnetite nanoparticles (Fe_3O_4 NPs) for separation are well established in biomedical applications,[12–14] as, for magnetite NPs of <100 nm size, their superparamagnetism allows for easy manipulation in low magnetic fields and separation from any background matrix.

Coating of Fe_3O_4 NPs with silica has been demonstrated for life sciences applications[12,15–19] and the removal of toxic heavy metal ions from water.[20–24] In these scenarios, the silica is applied as an inert barrier layer to protect the magnetite core in a range of pH environments.[25,26] However, the use of a silica-coated-magnetite system to address the structural integrity of cementitious infrastructures has not yet been reported. For this specific application, embedding a magnetic core into colloidal

[a]Department of Materials, Imperial College London, Exhibition Road, London SW7 2AZ, UK
[b]Department of Applied Science and Technology (DISAT), Politecnico di Torino, Corso Duca degli Abruzzi 24, 10129 Turin, Italy
[c]Department of Civil and Environmental Engineering, University of Strathclyde, James Weir Building, Level 5 75 Montrose Street, Glasgow G1 1XJ, UK
[d]London Centre for Nanotechnology, Imperial College London, Exhibition Road, London SW7 2AZ, UK. E-mail: eleonora.cali@polito.it; matteo.pedrotti@strath.ac.uk

silica offers the potential of controlled transport and emplacement of the SiO_2-coated Fe_3O_4 ($SiO_2@Fe_3O_4$) NPs *via* magnetic field manipulation. The presence of a magnetic core also means that neither a concentrated suspension nor a chemical accelerator is required for injection. Rather, we hypothesised that by using magnetic guidance to deliver the particles into a constrained geometry (the local crack), the field could then be used to overcome electrostatic interactions and drive gelling only within the crack.

In this work, we develop a water-dispersible superparamagnetic silica-coated magnetite ($SiO_2@Fe_3O_4$) nanoparticle system, which can be destabilized by magnetic field concentration to induce gelling. To mimic the effect of the ambient ions present in the real system, tests are also carried out in a NaCl electrolyte. Following characterization of the NPs pre- and post-gelling, further investigation is then carried out to evaluate the $SiO_2@Fe_3O_4$ NPs behaviour when driven through a simulated crack into cement *via* a magnetic field. We show that the $SiO_2@Fe_3O_4$ NPs are successfully driven to the desired location and gel only after correct emplacement, proving that the magnetic field concentration is sufficient to overcome the electrostatic repulsion.

2 Experimental and methods

2.1 Materials

2.1.1 SiO_2 coating of 12 nm Fe_3O_4 nanoparticles. Size controlled (12 nm) magnetite (Fe_3O_4) nanoparticles (NPs) were synthesized following a thermal decomposition method described in detail previously.[27] Encapsulation of the Fe_3O_4 NPs *in silica* shells was achieved through a reverse microemulsion method adapted from previous work.[28,29] 10 mL cyclohexane, 1.3 mg Igepal CO-520 (polyoxyethylene (5) nonylphenylether, Sigma-Aldrich) and 50 μl of DI H_2O were mixed at room temperature under vigorous stirring for the time required for the reverse microemulsion to become homogeneous. 3–4 nmol of oleic acid-capped Fe_3O_4 NPs concentrated in 1 mL of cyclohexane were subsequently added dropwise to the stirring mixture and equilibrated for 15 minutes. 80 μl of TEOS (99.999%, Sigma-Aldrich) and 150 μl of NH_3 H_2O (ACS reagent, Sigma-Aldrich) were subsequently added dropwise, separated by a mixing period of 15 minutes. The solution was kept under constant stirring at room temperature for 72 h. The resultant $SiO_2@Fe_3O_4$ NPs were recovered by washing with a mixture of absolute ethanol (≥99.8% AnalaR NORMAPUR ACS, VWR) and methanol (≥99.5% GPR RECTAPUR, VWR) for product precipitation, followed by centrifugation (4500 rpm, 30 minutes, 18 °C). After redispersion of the $SiO_2@Fe_3O_4$ NPs in ethanol, hexane was added to the product, which was subsequently centrifuged. The washing procedure was repeated at least six times to ensure purity, and the product stored in DI H_2O.

2.1.2 Portland cement preparation. Ordinary Portland Cement (Blue Circle 'General Purpose' Cement) was used to create two miniature vertical slabs (Fig. 1(a)) and three 'cracked' cylinders of cement (Fig. 1(b)). A 0.4 water to cement ratio was used, curing was performed at 20 °C in an insulated environment for the first 7 days and then air-dried up to a total of 28 days. For each specimen, about 25 mL of cement mixture were cast into a 50 mL Falcon centrifuge tube used as a mould. After curing, a simulated planar fracture along the longitudinal plane of the cylinders was created with a wedged section by means of an industrial water jet cutter (samples NM and S1).

2.2 Sample preparation

For each experiment, gel time was evaluated as the time required for the $SiO_2@Fe_3O_4$ suspension to form a visible, non-flowing gel under magnetic-field application, as assessed by macroscopic observation and photographic documentation upon inversion.

2.2.1 Gelling of $SiO_2@Fe_3O_4$ NPs in liquid through NaCl addition. To induce gelling of $SiO_2@Fe_3O_4$ NPs, model experiments were performed by evaluating the addition of an electrolyte accelerator to the colloid suspension (sample E in Fig. 1(a)). NaCl was used as accelerator in a 0.33 M final concentration, with a 5 : 1 volume ratio between the $SiO_2@Fe_3O_4$ NPs and the accelerator.[4] The mixtures were reacted for times ranging from 7 days to 14 days and aliquots of different contact time samples were diluted in DI H_2O and sonicated for 30 minutes, following dropcasting on TEM grids (holey carbon film copper grids, 3.05 mm diam., 300 mesh, TAAB) for microscopic characterization.

A zoom-in schematic of the NP circled in "NM" shows the structure of the core–shell NPs described in this work. The schematics represent the complementary analyses carried out to evaluate penetration and gelling performance of the material described in this work within the crack.

2.2.2 Gelling of $SiO_2@Fe_3O_4$ NPs through magnetic field application. Initiation of gelling through the sole presence of a magnetic field, without chemical initiator to screen the surface charge, was investigated by transferring an aliquot of $SiO_2@Fe_3O_4$ NPs dispersed in DI H_2O into a 25 mL Falcon centrifuge tube to which a NdFeB magnet was fixed on the side (sample "M" in Fig. 1(a)). The tube and magnet were left in position for 28 days, after which the magnet was removed and the sample sonicated in order to attempt redispersion of any ungelled NPs. The gelling efficiency was evaluated through dropcasting of the sonicated sample on a TEM grid and then characterized with a JEOL JEM 2100 F operated at 200 kV.

2.2.3 $SiO_2@Fe_3O_4$ in contact with a Portland cement -half section. A sample was prepared by using a vertical pouring section of Portland cement in contact with the $SiO_2@Fe_3O_4$ NP suspension (sample "B" in Fig. 1(a)). The cement section was fixed on the side of a Falcon centrifuge tube to occupy half the volume of the tube. This allowed evaluation of possible gelling effect on the NPs suspension of Ca^{2+} ions released by the cement into the water or present on the cement surface. To prevent the cement-suspension interaction from being driven by gravity, the centrifuge tube was kept in a vertical position (as shown in Fig. 1(a)). The sample was studied after 12 h of contact between the suspension and the cement.

2.2.4 $SiO_2@Fe_3O_4$ in contact with a Portland cement half-section with magnetic field application. The setup from subsubsection 1.2.3 was also used to study the combined effect of

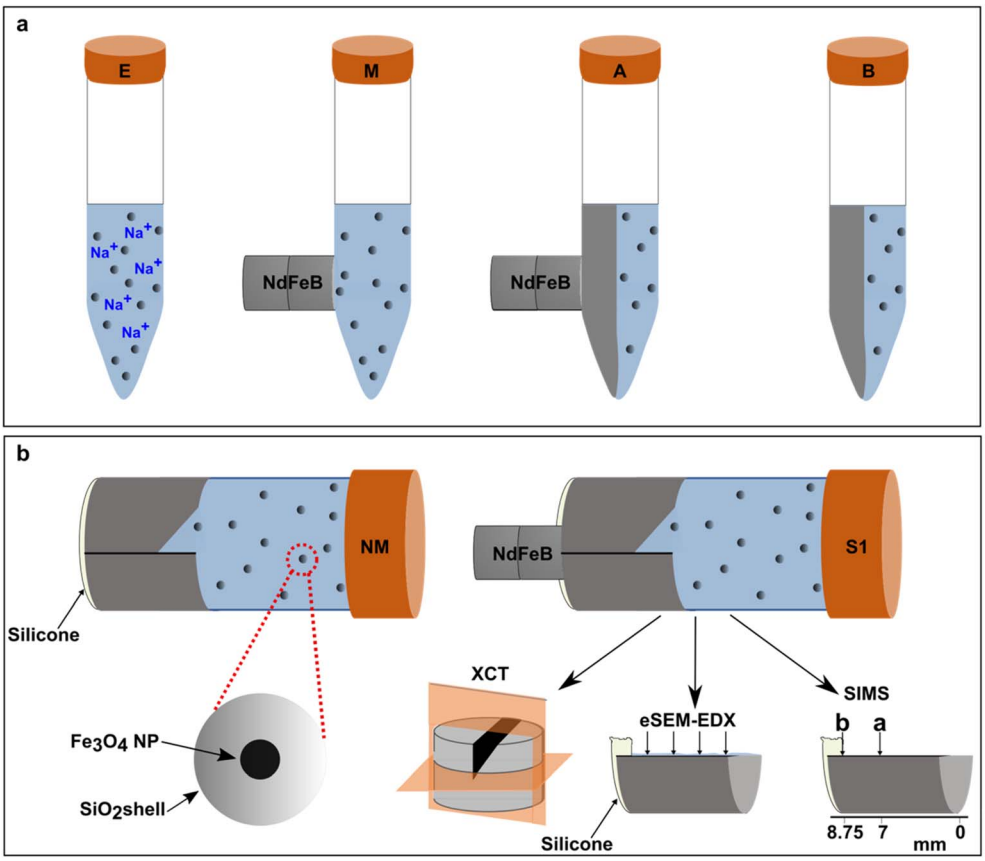

Fig. 1 Schematic representing the different sample setups described in this work; (a) shows the SiO_2@Fe_3O_4 NP suspension described in section 1.2.1–1.2.4, when: mixed with an electrolyte solution ("E"), a magnetic field was applied on the side of the container ("M"), a magnetic field was applied on the side of the container through the vertical half section of Portland cement ("A"), in contact with the vertical half section of Portland cement with no magnetic field ("B"); (b) shows the different crack geometries prepared for the experiments described in subsubsection 1.2.5: a cracked wedge sample with application of a magnetic field ("S1") and a control sample with no magnetic field application ("NM").

exposing simultaneously the NP suspension to a vertical cement surface (hence to Ca^{2+} ions) and to a magnetic field applied orthogonally to that surface (sample "A" in Fig. 1(a)). The sample was studied after 12 h of magnetic field application, when the magnet was removed and the sample sonicated for 10 minutes to attempt redispersion of any ungelled NPs.

2.2.5 Gelling of SiO_2@Fe_3O_4 NPs through simulated cracks in Portland cement *via* magnetic field application. A final model experiment was carried out by inducing flow of the SiO_2@Fe_3O_4 NPs through a simulated crack in a cementitious section. Fig. 1(b) presents a schematic of the experimental setups. Two different crack geometries were used for the experiment: a full section and a wedged section. The different geometries were used to evaluate the effects of surface geometry on NP flow through the crack, and any subsequent gelling, when applying a 0.48 T magnetic field. Finally, to study the effect of calcium (Ca^{2+}) ions present in the cement on the NP gelling behaviour, an identical control experiment was carried out using the wedge-cracked cement section without applied magnetic field. For this series of geometries, water sealing between the Falcon tubes and the cement cylinders was provided by a rubber O-ring and an external layer (approx. 1 mm) of commercial silicone gel sealant.

2.3 Sample characterization

The gelling efficiency (of the SiO_2@Fe_3O_4 NPs) in each experiment described above was investigated at the macroscale through a Nikon XT H 225 LC X-ray computed tomography system and at the micro/nano-scale with a JEOL JEM-2100 F and a JEOL JEM 2100Plus TEMs operating at a 200 kV voltage, taking advantage of the high-contrast given by the Fe-based NP cores with respect to sole SiO_2. After addition of NaCl, the samples were prepared for TEM analysis with a 1 : 1000 dilution of the original electrolyte-added sample followed by ultrasonication in order to avoid possible artefacts due to drying effects when depositing concentrated samples on to the grid. The SiO_2@Fe_3O_4 NPs penetration within the crack was studied using an environmental SEM (eSEM, Quanta 650 FEG) coupled with EDS detector (XFlash 6160). The eSEM was operated at 800 Pa to prevent drying of the analysed samples and avoid consequent artefacts. High-resolution SEM imaging was carried out with a Zeiss Auriga featuring a Schottky field emission gun operating at 5 kV. High resolution time-of-flight secondary ion mass spectrometry (ToF-SIMS) was carried out using an IONTOF ToF-SIMS 5 instrument to evaluate the penetration of the nanoparticles through the cement crack. The analytical ion beam used was a 25 keV Bi^+ LMIG, in high current bunch mode

with a beam current of ~1 pA. The analytical area was 50 mm^2. Positive secondary ions were collected, for a total of 100 scans. After each analysis, the sample was then moved a further 0.25 mm away, and another mass spectrum collected. The secondary ion counts were then normalised to the total ion counts obtained in each analysis, and the Fe^+ secondary ion counts were then plotted as a distance in mm, from the edge of the cross-section.

3 Results and discussion

3.1 SiO_2@Fe_3O_4 NP characterisation

TEM micrographs of the coated NPs obtained by applying the optimised microemulsion procedure are reported in Fig. 2(a–c). After 72 hours of reaction, a homogeneous coating of 17.3 ± 2.0 nm was obtained on the 12 nm Fe_3O_4 NPs. The microemulsion coating method resulted in single-core structures with high control over the SiO_2 shell sizes and coating efficiency, with no SiO_2 core-free particles observed (analysis based on $n = 253$ imaged NPs). The method allows for the formation of aqueous micelles in an organic solvent, allowing for; the formation of nanoreactors where the growth of silica shells around the initially hydrophobic magnetic NP cores is achieved, according to La Mer theory.[28,30–32] The NPs suspension shows a high degree of dispersion, visible from Fig. 2(a–c). The pH of the SiO_2@Fe_3O_4 NP samples prior to addition of accelerator was measured as 6.58 (pH meter, Inolab pH 7310, WTW). At near-neutral pH the SiO_2 NP liquid suspension is characterised by surface Si–O– functional groups, since the pH is higher than the point of zero-charge (pzc_{SiO_2} = pH 2).[9,10] No agglomeration is indeed observed by imaging and evidence of numerous isolated NPs was found (Fig. 2(c)), expected due to the strong electrostatic repulsion generated by the formation of an electrical double layer surrounding the SiO_2 NPs dispersed in a polar medium (water in the case presented here). This is confirmed by a size distribution of 51.7 ± 3.9 nm of the NPs measured from TEM images, which agrees well with that measured by Dynamic Light Scattering (DLS) (SI Fig. S2, average diameter = 53.1 ± 10.3) and confirms that the colloids remain stable (no agglomeration or gelling is observed).

3.2 Gelling of SiO_2@Fe_3O_4 NPs by electrolyte addition

The effect of adding a 2 M NaCl solution to SiO_2@Fe_3O_4 NPs in a 1 : 5 ratio was examined at two time points by collecting aliquots of the sample after 7 and 14 days. Fig. 2(d and e) show NPs from the aliquot collected after 7 days, and Fig. 2(f) after 14 days upon addition of the electrolyte. Upon destabilization by the electrolyte, extensive growth of inter-particle connections is observed by the presence of "necks" in the contact areas between the different coatings when compared to the as-synthesized NPs (Fig. 2(a–c)), indicating direct interaction of the Si–O– functionalities on the NP surfaces. Specifically, in Fig. 2(d–f) the Fe_3O_4 cores are still easily differentiable, however the morphology of the SiO_2 coatings has changed from spherical shells to an interconnected network, due to the formation of Si–O–Si bonds in-between NPs. This is caused by the increase in the ionic strength of the host solution caused by the addition of the electrolyte, resulting in charge screening and an increased probability of NP collision, and hence of gelling. Imaging multiple aliquots from the same sample confirmed that gel formation occurred within the first 7 days.

3.3 Gelling of SiO_2@Fe_3O_4 NPs by magnetic concentration

Fig. 3 shows the effect of applying a magnetic field on a diluted suspension of as-synthesized SiO_2@Fe_3O_4 NPs for 28 days. The

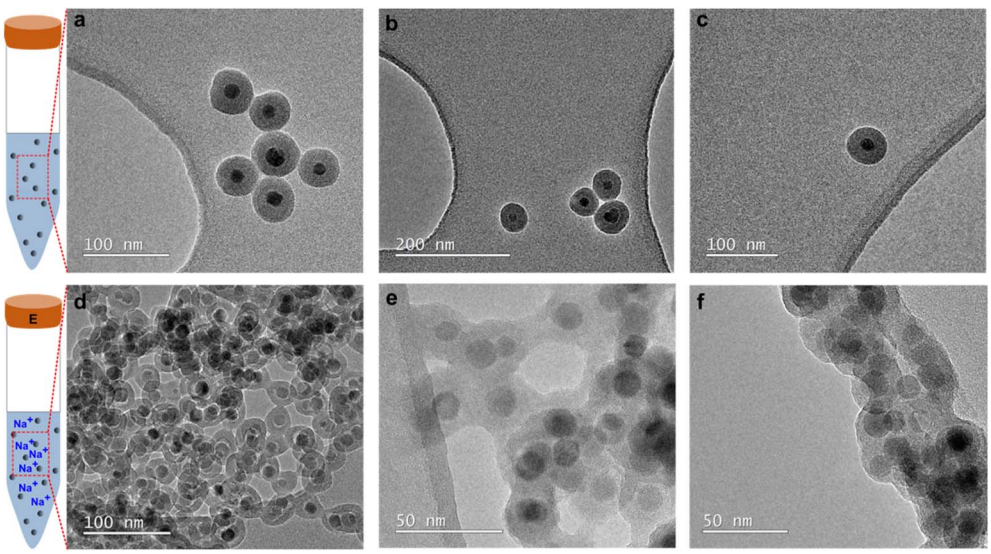

Fig. 2 (a–c) TEM micrographs of SiO_2@Fe_3O_4 NPs obtained by applying the microemulsion method described in this work. Homogeneous, core-centred coated NPs are obtained, characterized by high dispersibility. (d–f) TEM micrographs of the coalesced silica shells after addition of a 2 M NaCl solution to a SiO_2@Fe_3O_4 NPs sample. (d and e) Were collected after 7 days and (f) after 14 days upon NaCl solution addition, respectively. Gelling of the silica shells is evidenced by the visible silica network embedding the Fe_3O_4 cores. Sample preparation was performed by dilution of an aliquot of the gelled sample followed by ultrasonication for 10 minutes. Features characterizing the gelled SiO_2@Fe_3O_4 NPs after 7 and 14 days of the addition of the electrolyte are mostly similar.

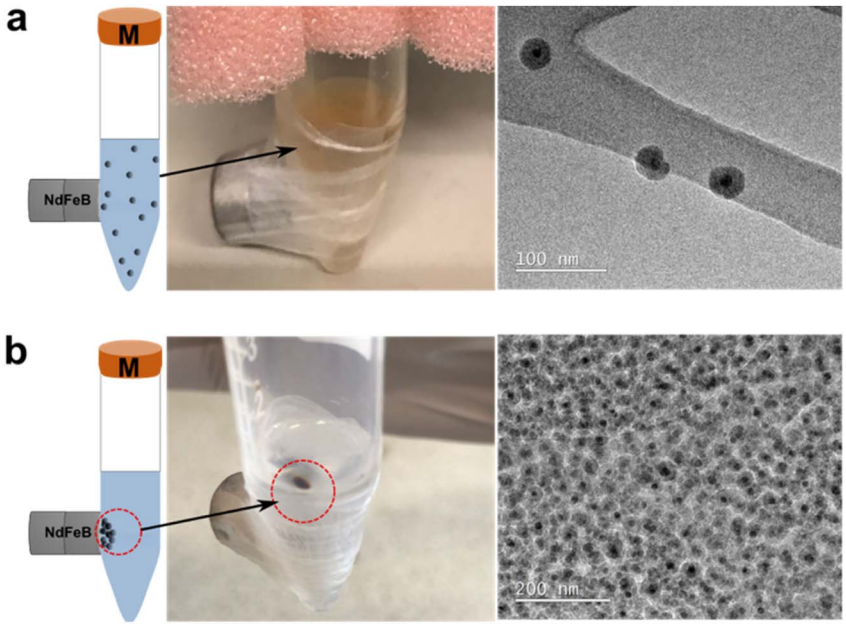

Fig. 3 (a) Image and corresponding TEM micrograph of the as-prepared SiO_2@Fe_3O_4 NPs suspension upon application of a magnetic field (the NdBFe magnet is fixed on the side of the suspension container to counteract gravity effect); (b) image and corresponding TEM micrograph of the same suspension presented in (a) after 28 days of application of the magnetic field showing NP concentration and gelling.

starting suspension (Fig. 3(a)) is characterized by dispersed NPs at near-neutral pH, as confirmed by the observed pale-brown colour of the suspension and by TEM imaging, showing the expected high degree of dispersion. Upon application of a magnetic field for 28 days, concentration of the magnetic NPs is visible, and coalescence of the SiO_2 shells was confirmed by TEM (Fig. 3(b)), proving that gelling can also be induced by concentration of the NPs through the application of a magnetic field.

3.4 Gelling of SiO_2@Fe_3O_4 NPs by magnetic concentration on cement geometries

The first experiment used two half-cylinders of Portland cement in contact with the SiO_2@Fe_3O_4 NP suspension (Fig. 4). A 0.48 T NdFeB magnet was applied on the side of "sample A" to study the combined effect on the gelling phenomenon of the magnetic field and on the leaching of cations from the cement (Fig. 4(a)). Upon 12 h of magnetic field application, a gel formed on the cement surface of "sample A" (Fig. 4(a and b)), which is retained even after ultrasonication (10 min) ("Sample A" in Fig. 4(c)), confirming the non-reversibility of the process. A control sample ("sample B", Fig. 4(c)) was prepared to evaluate the effect of Ca^{2+} leaching-only from the cement surface on the NP suspension. The colour difference of the liquids in "sample A" and "sample B" in Fig. 4(c) is due to the different behaviour of the NPs in the presence/absence of the magnetic field. The clear surrounding solution of "sample A" indeed results from the majority of the NPs having gelled on the cement surface. In "sample B", only a thin NP layer was found on the cement surface and gelling did not occur; NPs remain dispersed even after 12 h of contact, as visible from the uniform pale-brown colour of the liquid, very similar to the colour of the slightly more concentrated initial suspension in Fig. 4(b).

3.5 *In situ* characterisation of gelled SiO_2@Fe_3O_4 NPs within cement cracks

To study the possibility of achieving macroscopically appreciable gel formation inside Portland cement cracked sections, a proof-of-concept was developed by carrying out the same experiment using two half-cylinders of cement placed edge-to-edge down one of the long sides, creating a wedge-shaped crack (see "S1" schematics in Fig. 1(b)). After application of a 0.48 T magnetic field orthogonal to the cracked cement surface, the sample was stored horizontally to avoid any effect other than the magnetic field on the NPs motion. To evaluate the gelling efficacy due to the magnetic force, as opposed to the positive ions present in the cement (*e.g.*, Ca^{2+}), a control sample ("NM" in Fig. 1(b)) was prepared without applying any magnetic field.

Samples observed after 5 days of magnetic field application showed formation of a viscous gel on the surface of the cement cylinder, leaving a clear aqueous solution when compared to the starting suspension (SI Fig. S1(a and b), respectively). This was, however, not the case for the NM sample, where the suspension retained its original colour after the same 5 day-period (SI Fig. S1(d and e)). The sample was sealed to inhibit water evaporation, and no NP mobility was observed upon inversion of the test tube, therefore confirming gelling of the SiO_2@Fe_3O_4 NPs. To study the NPs transport through the crack and to evaluate possible penetration in the cement pores (orthogonal to the crack), samples S1 and NM were analyzed using Xray-Computer Tomography (X-CT). SI Fig. S1(c) and (f) show the two samples

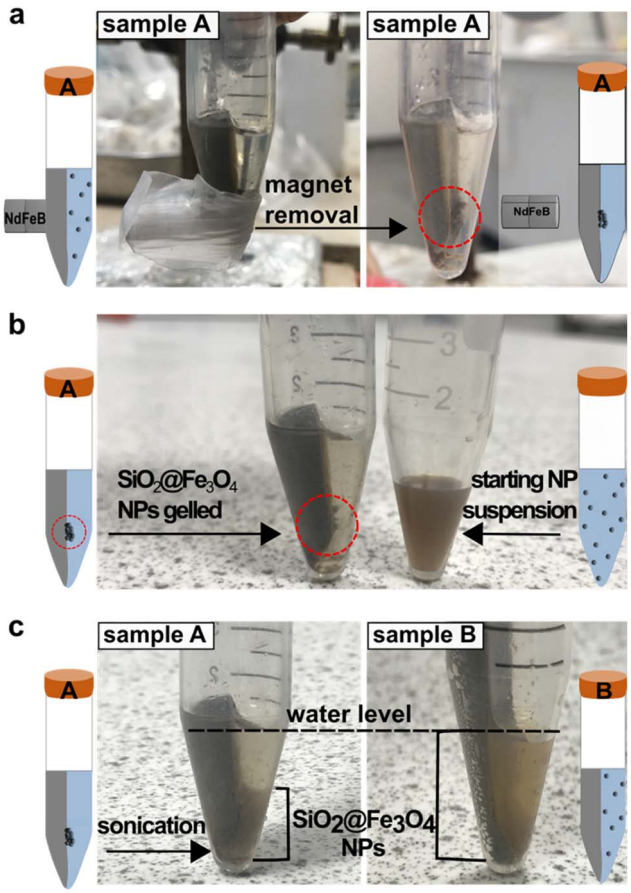

Fig. 4 (a) Image of "sample A" described in subsubsection 1.2.4 before (left-hand side) and after (right-hand side) removing the magnetic field. The magnet was applied on the side of the Falcon tube through the vertical pouring cement half-section. When removing the magnet after 12 h a gel was observed on the cement surface in correspondence to the magnet position (circled in red). (b) Comparison of the gelled NPs in "sample A" after removal of the magnet from the side of the cement pouring (left-hand side) and a starting NP suspension (right-hand side). The difference in the colour of the initial suspension highlights the occurred gelling of "sample A". (c) Images of samples described in subsubsection 1.2.4 and subsubsection 1.2.3, with ("sample A") and without ("sample B") magnetic field application respectively) after 12 h of the NPs being in contact with the cement. After magnetic field removal "sample A" was sonicated to redisperse ungelled NPs. The water colour difference in the two samples results from gelling of "sample A" as opposed to "sample B", where no gelling occurred.

prior to water removal before the analysis, where the macroscopic colour difference between the two suspensions, transparent for S1 and brown for NM, is clearly evident.

Fig. 5 shows a series of cross-sections extracted from the X-CT scan on samples S1 and NM. Fig. 5(a) shows a horizontal cross-section of sample S1. A solid gel is clearly visible on top of the vertical right surface, where the SiO_2 suspension was in direct contact with the cementitious paste (lilac area in the image). It should be noted that this lilac highlighting is used to aid the visualization of the silica phase and is not meant to be quantitative. Interestingly, the macro-pores within the cement paste are partially filled by solidified gel. Looking at the magnified image in Fig. 5(b) it appears that smaller pores achieved a better filling than larger ones. Fig. 5(c and d) show two vertical cross-sections at different distances from the right interface, the former being closer than the latter. At a short distance from the wedged section entrance, the gel entirely filled the wedged surface. As the wedge becomes narrower, air appears to remain trapped, preventing a homogeneous filling of the crack (Fig. 5(d)). The results shown in the magnified image in Fig. 5(e) suggest that a better pore filling is achieved closer to the wedge. Empty or partially filled pores start appearing as one moves away from the wedge. Similarly, Fig. 5(f) (cross-section through the bottom of the crack) shows that only partial pore filling was achieved in this region. Again, smaller pores show a better filling than larger ones.

Fig. 5(g and h) show two horizontal cross-sections of sample NM (no magnetic field applied). The horizontal cross-section in Fig. 5(g) is orthogonal to the wedged crack while the one in Fig. 5(h) is parallel. Interestingly, even though no magnetic field was applied for this sample, the gel was found on the entire wedged surface. As seen in both horizontal sections, some spherical pores appear to have been filled by the SiO_2 gel. In contrast with sample S1, neither the distance from the top surface nor the distance from the wedged surface seems to affect the amount of filled pores; however, also for sample NM smaller pores show a better filling than larger ones (Fig. 5(i)).

Governed by the Young-Laplace principle, capillary pressure increases as pore size decreases, meaning small pores are expected to fill before larger ones under a negative hydraulic potential. This observation suggests that the SiO_2@Fe_3O_4 NP penetration into the cement could be driven solely by the hydraulic gradient between the dry cement and the suspension, rather than by the magnetic potential. To explore this theory, Fig. 6 reports the measured initial porosity of samples S1 and NM, *i.e.*, ~3%, calculated as the ratio between the volume of voids and the volume of solids as determined from the X-CT scans. To ensure the robustness and reproducibility of these calculations, a variance of ±5 grayscale values was applied to the manually selected segmentation threshold. The minimal impact of this variance on the calculated porosity is reflected by the error bars included in the plot. Upon exposure to the SiO_2@Fe_3O_4 NP suspension, the porosity in sample NM decreased only to a value of 2.5%, whereas the porosity in sample S1, where the magnetic field was applied, decreased to a value <1.5%, halving the available pore space. This suggests that the magnetic field does indeed increase the number of NPs that have penetrated the cement.

To confirm the observation from the X-CT scans that NP penetration occurred through the cement, SEM analysis of the wet S1 sample in environmental mode was carried out using an 800 Pa pressure to minimize water evaporation within the sample and to disregard SiO_2 gelling due to drying artefacts.[33] Specifically, after X-CT scans were performed, the sample was removed from the aqueous medium before SEM analysis (SI Fig. S1(c)) and imaging was carried out on the surface of the cement section, first near the crack (without disassembling the cement sections), as well as at the cross-section (after separating the cement half-sections), as presented in the schematic

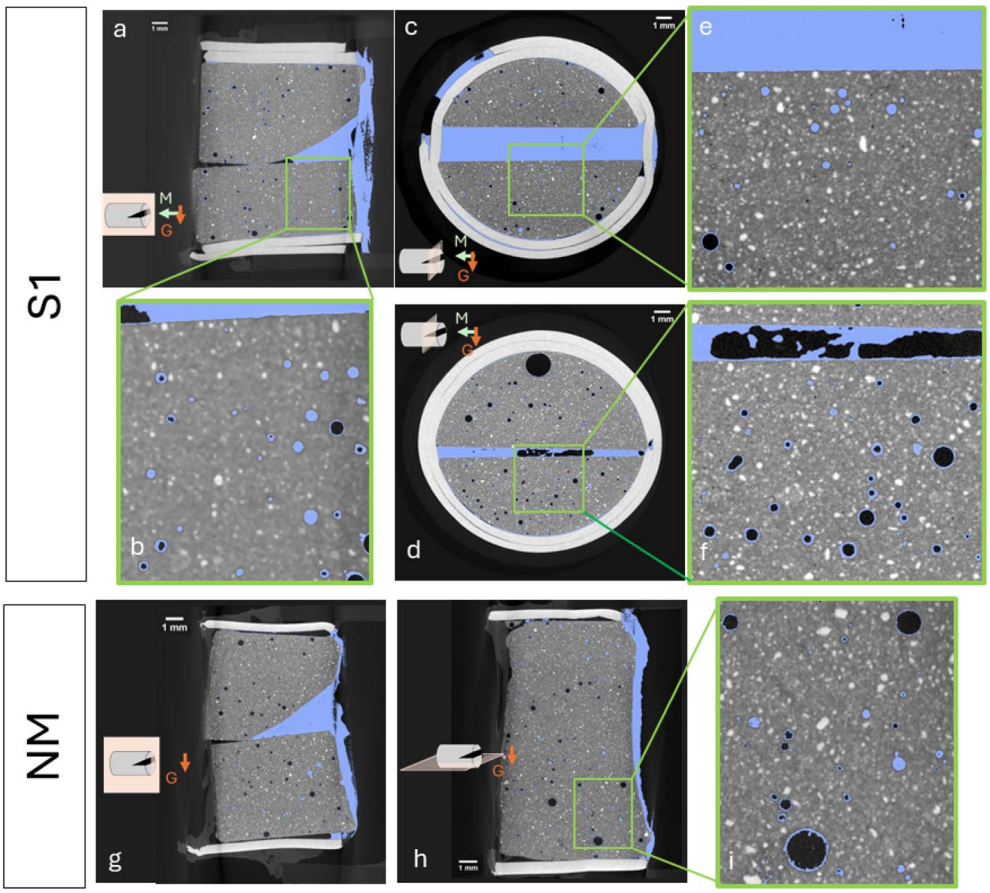

Fig. 5 X-CT scan of sample S1 and NM (no magnetic field applied). Any remaining suspension was removed before X-CT scan and the sample was scanned upside-down, in order to make sure that any phase found on the cement surface was gelled (*i.e.*, a solid phase). The segmented magnetite-silica phase is shown in lilac for visualization purposes only to increase the contrast against the cementitious and the air phase and is not quantitative. (a) Vertical cross section of sample S1 showing solid gel formation at the surface where the cement-colloidal suspension interface was present. (b) A 4X magnification of the area near the wedge showing most of the pores filled by silica gel. (c) A horizontal cross-section of sample S1 taken close to the top surface (cement – silica suspension interface) showing the wedged area to be filled by colloidal silica. (d) A horizontal cross-section of sample S1 taken at the bottom of the wedged section showing partial filling of the wedged section. (e) and (f) A 4X magnification of the area near the wedge boxed in figure (c) and (d) respectively. (g) Sample NM (cross-section plan is transversal to the wedge plan); (h) vertical cross-section of sample NM (cross-section plan is parallel to the wedged plan), (i) a 4X magnification of the boxed area. Unaltered version of Figure a, c, d, g and h is shown in SI Fig. S3.

reported in Fig. 1(b). The secondary electron images (Fig. 7(a–d)), show the presence of a gel network both on the surface and throughout the entire crack. Fig. 7(a and b) show the microstructure of the gelled sample at the crack surface and 5 mm in depth inside the crack, respectively. A uniformly distributed gel is evidently present within the crack. To study the penetration depth of the SiO_2@Fe_3O_4 NPs through the length of the crack, the section was subsequently opened for EDS maps to be collected along the crack. EDS analysis showed presence of Fe uniformly distributed across the crack, confirming homogeneous penetration of the NPs into the crack (Fig. 7(e–h)). Fig. 8(a) shows the EDS analysis carried out on a 3.5 mm longitudinal cross-section along the crack. Maps acquired on the region boxed in Fig. 8(b), reported at higher magnification in Fig. 8(c), revealed homogeneous distribution of Fe, Si, and O along the analysed region (Fig. 8(d–f), respectively). The NP flow caused by the applied magnetic field is indicated by the arrow in

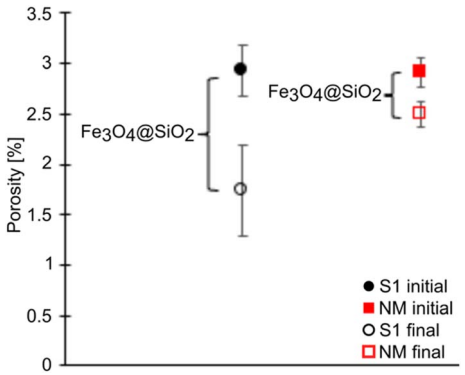

Fig. 6 Plot of the calculated porosity for sample S1 and NM. The initial porosity was calculated as the pore space occupied by both silica matrix and air over the total volume. The final porosity is calculated by considering only the pore space filled by air over the total volume. For each point, error bars represent the minimum and maximum calculated porosity resulting from a centred range of threshold values of ±5 intensity units.

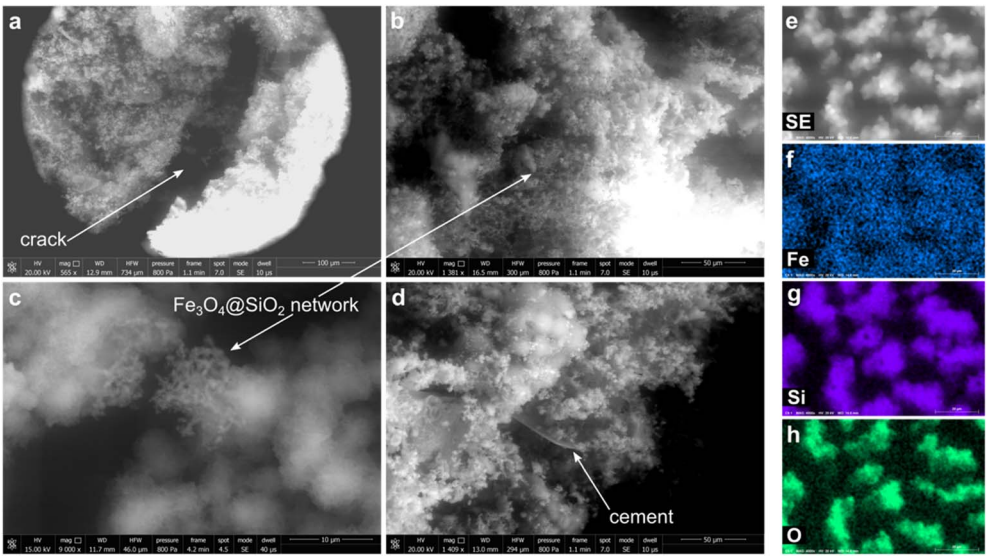

Fig. 7 (a) Secondary electron SEM image of the top of the cylindrical section showing presence of gel in the crack; (b–d) SEM characterization of the network of SiO_2@Fe_3O_4 gel obtained on the cementitious section within the crack; (e) secondary electron image of gelled SiO_2@Fe_3O_4 NPs within the cement crack and corresponding elemental maps obtained by EDS of (f) Fe, (g) Si, and (h) O, respectively. The more diffuse Fe elemental map compared to the Si and O ones is due to the lower Fe content associated with the Fe_3O_4 cores relative to the SiO_2 shells and to spatial averaging in the eSEM–EDS measurements at 800 Pa.

Fig. 8(b), and the maps were acquired from a region close to the crack edge ("crack origin" in (b)) to the bottom of the crack, as indicated by the presence of the sealant. A concentration gradient in iron (or SiO_2) was not observed (Fig. 8(d–f)), confirming that penetration of the NPs through microsized cracks can indeed occur even with only a 0.48 T applied magnetic force.

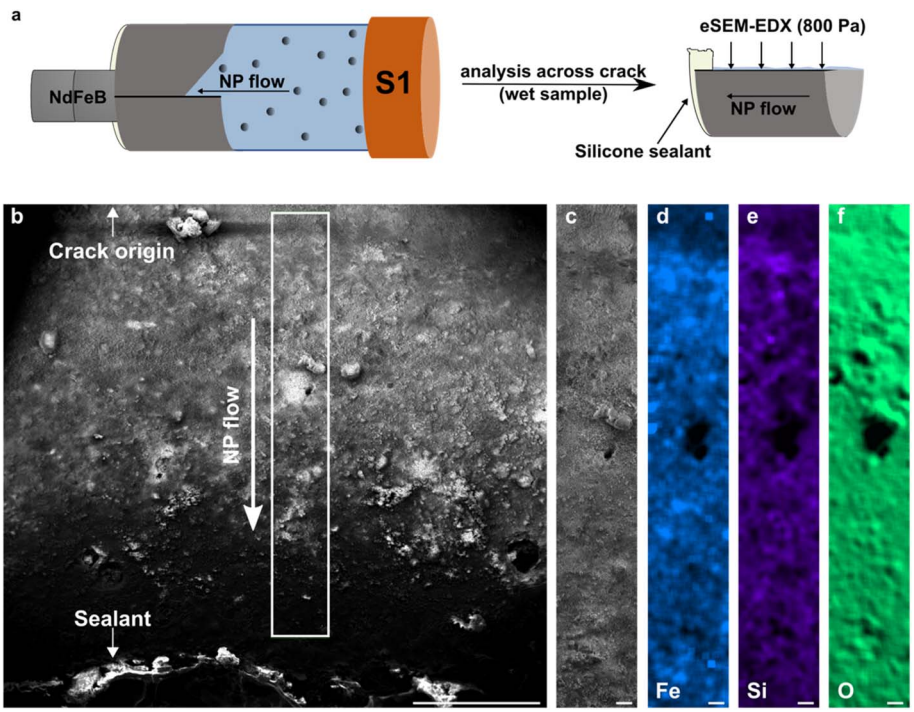

Fig. 8 (a) Schematic of the EDS analysis carried out on sample S1 by eSEM. (b) Secondary electron image acquired on a longitudinal cross-section of the gelled SiO_2@Fe_3O_4 NPs through the cracked cement. EDS mapping was carried out on the boxed region to evaluate possible Fe concentration gradient from a region closer to the crack initiation ("crack origin") to the end of the crack (showed by presence of the "sealant"), where the magnet was fixed. The arrow shows the direction of the NP flow through the crack; (c) SEM image of the longitudinal cross-section boxed in (b) and corresponding (d) Fe, (e) Si, and (f) O EDS maps, respectively. The scalebars are 1000 μm in (a) and 90 μm in (b–e).

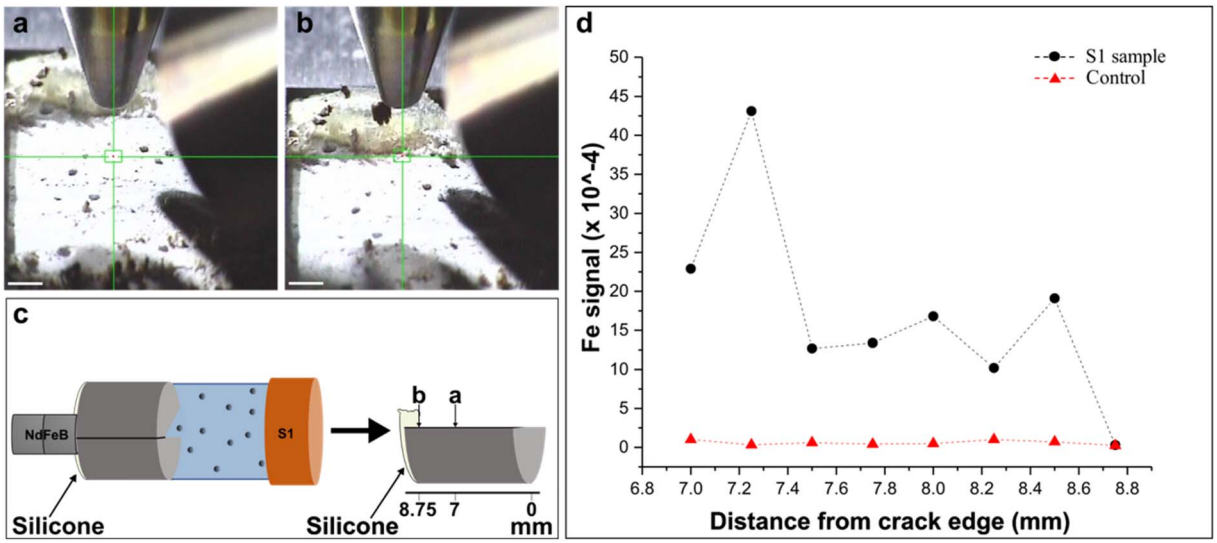

Fig. 9 High-resolution ToF-SIMS analysis of the longitudinal cross-section along the crack. Positive secondary ions were collected for a total of 100 scans per point. After each analysis, the sample was moved a further 0.25 mm away, where another mass spectrum was collected. (a) and (b) Show the start and end collection points on the analyzed sample, and are shown in the schematics in (c): the cement cylinder was disassembled along the crack depth and the analysis was performed on one of the half-sections from sample S1. Points "a" and "b" were acquired at 7 mm and 8.75 mm from the crack initiation, respectively. Secondary ion counts were normalized to the total ion counts obtained in each analysis, and in (d) the Fe^+ counts are plotted as a distance in mm from the edge of the cross section (black plot). An as-prepared cement sample was also analyzed as a control to evaluate Fe^+ contribution before NP addition (red plot). Scalebar in (a) and (b) is 1 mm.

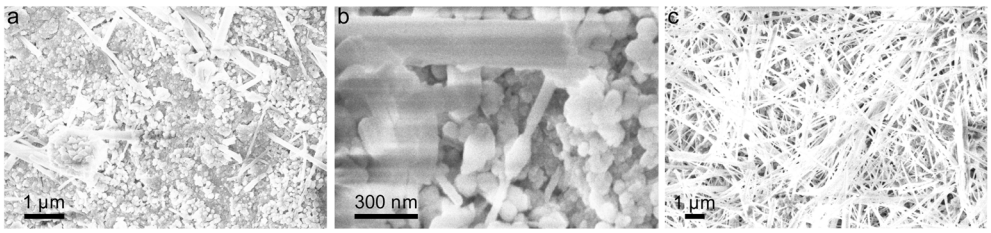

Fig. 10 Secondary electron high-resolution SEM images obtained on sample S1 showing the different morphologies observed for the gelled material within the crack. (a) Spherical NPs and needle-like structures are visible; (b) higher resolution image showing the spherical morphology of the SiO_2@Fe_3O_4 NPs is noticeable after gelling; (c) Dense network of needle-like structures found within the gelled material.

3.6 Postmortem characterisation of gelled SiO_2@Fe_3O_4 NPs in cement

To better evaluate and confirm the penetration and gel thickness of the NPs, ToF-SIMS analysis was performed, and the results are reported in Fig. 9. Mass spectra were acquired on the surface of the sample's cross-section at 7.00 mm distance from the crack origin (Fig. 9(a)) to 8.75 mm (Fig. 9(b)), with the last data point acquired on the sealant, also shown in the schematics in Fig. 9(c). Fig. 9(d) shows the Fe^+ secondary ion counts plotted against the distance from the crack, where a mass spectrum was obtained every 0.25 mm over the analysed section. Fe^+ secondary ions are consistently detected throughout the surface, dropping to 0.295×10^{-4} only at the crack end. These data are consistent with results obtained with SEM-EDS, with Fe^+ homogeneously detected throughout the entire analysed surface, confirming complete filling of the crack. To evaluate the possible Fe contribution from the as-prepared cement, a control sample was also analyzed. The Fe^+ secondary ion counts were found to be an order of magnitude smaller, at $0.598 \pm 0.29 \times 10^{-4}$ over the same longitudinal section of the control sample (Fig. 9(d)).

Finally, high-resolution SEM was carried out on the dried samples and showed presence of different morphologies through the material gelled within the crack. Fig. 10(a and b) show evidence of both spherical NPs and needle-like structures for this sample. Fig. 10(c) shows an SEM image acquired towards the central section of the crack in sample S1, where a dense needle-like network was mostly present, resembling C–S–H (calcium silicate hydrate) crystals.[34–37] These results hence suggest that Ca may be incorporated into this network.[1,38]

Our results highlight the possibility of magnetically-driven SiO_2@Fe_3O_4 NPs to specific defect areas, resulting in subsequent NP gelling. The NPs presented in this work could be applied to cracked grouted waste forms. The cement layer, characteristic of grouted waste drums is easily obtained using magnetic fields, with the thickness of the concrete not posing

a limit to the emplacement of the NPs for the studied experiments. Compared to the use of pure SiO_2 nanocolloids in the field application scenario, our results prove that the presence of a magnetic core eliminates the issue of requiring a starting concentrated suspension to inject: a dilute suspension of SiO_2@Fe_3O_4 NPs can be used, and the application of a local magnetic field eventually results in the core–shell NPs concentration locally increasing at the site of interest and, consequently, after, in their gelling.

4 Conclusions

The results obtained in this work show the potential of using SiO_2@Fe_3O_4 NPs for addressing challenges related to the structural integrity of cement structures. The application of an optimised microemulsion strategy to obtain the SiO_2 coating results in hydrophilic, highly stable, and homogeneously coated SiO_2@Fe_3O_4 NPs characterised by a 1 : 1 core/shell ratio.

It was demonstrated that gelling of the SiO_2@Fe_3O_4 NPs developed in this work can be obtained solely by magnetic concentration. The applied magnetic field effectively overcomes the electrostatic repulsion between the NPs, entirely eliminating the need for electrolyte addition to trigger the sol–gel transition. This shift from chemically-induced to physically-induced gelling yields practical implications, particularly for sensitive environmental applications such as radionuclide containment infrastructure. Bypassing electrolyte use (such as NaCl) prevents severe collateral damage, including the chloride-induced corrosion of embedded metals and the competing action of Na^+ ions that can increase radionuclide desorption.

Furthermore, the magnetic drive allows for the use of highly diluted suspensions to achieve precise concentrations exactly where needed. This eliminates the need for high-pressure hydraulic injection, thereby reducing the risk of crack propagation, and opens the possibility of remotely guiding the SiO_2@Fe_3O_4 NPs through bulk bodies of water like storage ponds.

Finally, the contrast observed in X-ray CT results also highlights that 3D mapping of the gel distribution and crack filling behaviour can be obtained non-destructively on deteriorating cement infrastructure, offering valuable insights into the internal healing mechanisms and enabling more effective assessment of durability and performance over time.

Conflicts of interest

The authors declare that the research was conducted in the absence of any commercial or financial relationships that could be construed as a potential conflict of interest.

Data availability

The primary data supporting the findings of this study, including experimental protocols and chemical characterization, are available within the article and its supplementary information (SI). Due to the significant file size and dimensionality of the raw X-ray Computed Tomography (X-ray CT) datasets, these are not hosted in the SI but are available from the corresponding author(s) upon reasonable request.

Supplementary information is available. See DOI: https://doi.org/10.1039/d6ta01009a.

Acknowledgements

This work was performed as part of the EPSRC-funded Distinctive Research Programme. M. P. Ryan is supported by a Royal Academy of Engineering/Shell Research Chair for Interfacial Nanoscience.

References

1 D. Kong, *et al.*, Effect and mechanism of colloidal silica sol on properties and microstructure of the hardened cement-based materials as compared to nano-silica powder with agglomerates in micron-scale, *Cem. Concr. Compos.*, 2019, **98**, 137–149.
2 B. Pomaro, A Review on Radiation Damage in Concrete for Nuclear Facilities: From Experiments to Modeling, *Model. Simul. Eng.*, 2016, **2016**, 4165746.
3 M. Pedrotti, C. Wong, G. El Mountassir, J. C. Renshaw and R. J. Lunn, Desiccation behaviour of colloidal silica grouted sand: A new material for the creation of near surface hydraulic barriers, *Eng. Geol.*, 2020, **270**, 105579.
4 M. Pedrotti, C. Wong, G. El Mountassir and R. J. Lunn, An analytical model for the control of silica grout penetration in natural groundwater systems, *Tunn. Undergr. Space Technol.*, 2017, **70**, 105–113.
5 C. Wong, M. Pedrotti, G. El Mountassir and R. J. Lunn, A study on the mechanical interaction between soil and colloidal silica gel for ground improvement, *Eng. Geol.*, 2018, **243**, 84–100.
6 R. Maddalena and A. Hamilton, Low-pressure silica injection for porosity reduction in cementitious materials, *Constr. Build. Mater.*, 2017, **134**, 610–616.
7 P. Bots, *et al.*, Geochemical evidence for the application of nanoparticulate colloidal silica gel for *in situ* containment of legacy nuclear wastes, *Environ. Sci. Nano*, 2020, **7**, 1481–1495.
8 P. Persoff, J. Apps, G. Moridis and J. M. Whang, Effect of dilution and contaminants on sand grouted with colloidal silica, *J. Geotech. Geoenviron. Eng.*, 1999, **125**(6), 461–469.
9 J.-E. Otterstedt, and D. A. Brandreth, *Small Particles Technology*, Springer US, Boston, MA, 1998, DOI: 10.1007/978-1-4757-6523-6.
10 R. K. Iler, *The Chemistry of Silica*, Wiley, New York, 1979.
11 A. G. Pagano, G. El Mountassir and R. J. Lunn, Performance of colloidal silica grout at elevated temperatures and pressures for cement fracture sealing at depth, *J. Pet. Sci. Eng.*, 2022, **208**, 109782.
12 A. K. Gupta and M. Gupta, Synthesis and surface engineering of iron oxide nanoparticles for biomedical applications, *Biomaterials*, 2005, **26**, 3995–4021.

13 S. Mornet, S. Vasseur, F. Grasset and E. Duguet, Magnetic nanoparticle design for medical diagnosis and therapy, *J. Mater. Chem.*, 2004, **14**, 2161–2175.
14 Q. A. Pankhurst, J. Connolly, S. K. Jones and J. Dobson, Applications of magnetic nanoparticles in biomedicine, *J. Phys. Appl. Phys.*, 2003, **36**, R167.
15 A. del Campo, T. Sen, J.-P. Lellouche and I. J. Bruce, Multifunctional magnetite and silica–magnetite nanoparticles: Synthesis, surface activation and applications in life sciences, *J. Magn. Magn. Mater.*, 2005, **293**, 33–40.
16 J. M. Rosenholm, J. Zhang, W. Sun and H. Gu, Large-pore mesoporous silica-coated magnetite core-shell nanocomposites and their relevance for biomedical applications, *Microporous Mesoporous Mater.*, 2011, **145**, 14–20.
17 J. Kim, *et al.*, Multifunctional uniform nanoparticles composed of a magnetite nanocrystal core and a mesoporous silica shell for magnetic resonance and fluorescence imaging and for drug delivery, *Angew Chem. Int. Ed. Engl.*, 2008, **47**, 8438–8441.
18 J. Guo, W. Yang, C. Wang, J. He and J. Chen, Poly(N-isopropylacrylamide)-Coated Luminescent/Magnetic Silica Microspheres: Preparation, Characterization, and Biomedical Applications, *Chem. Mater.*, 2006, **18**, 5554–5562.
19 D. H. Lee, *et al.*, Enhanced Cellular Uptake of Silica-Coated Magnetite Nanoparticles Compared with PEG-Coated Ones in Stem Cells, *J. Nanosci. Nanotechnol.*, 2015, **15**, 5512–5519.
20 S. Sadeghi, H. Azhdari, H. Arabi and A. Z. Moghaddam, Surface modified magnetic Fe3O4 nanoparticles as a selective sorbent for solid phase extraction of uranyl ions from water samples, *J. Hazard. Mater.*, 2012, **215–216**, 208–216.
21 P. I. Girginova, *et al.*, Silica coated magnetite particles for magnetic removal of Hg2+ from water, *J. Colloid Interface Sci.*, 2010, **345**, 234–240.
22 M. R. Shishehbore, A. Afkhami and H. Bagheri, Salicylic acid functionalized silica-coated magnetite nanoparticles for solid phase extraction and preconcentration of some heavy metal ions from various real samples, *Chem. Cent. J.*, 2011, **5**, 41.
23 C. Huang and B. Hu, Silica-coated magnetic nanoparticles modified with γ-mercaptopropyltrimethoxysilane for fast and selective solid phase extraction of trace amounts of Cd, Cu, Hg, and Pb in environmental and biological samples prior to their determination by inductively coupled plasma mass spectrometry, *Spectrochim. Acta, Part B*, 2008, **63**, 437–444.
24 S. Bao, *et al.*, Highly selective removal of Zn(II) ion from hot-dip galvanizing pickling waste with amino-functionalized Fe_3O_4@SiO_2 magnetic nano-adsorbent, *J. Colloid Interface Sci.*, 2016, **462**, 235–242.
25 L. Vivar Mora, *et al.*, Influence of silica nanoparticles on corrosion resistance of sol-gel based coatings on mild steel, *Surf. Coat. Technol.*, 2017, **324**, 368–375.
26 S. Aberdeen, C. A. Hur, E. Cali, L. Vandeperre and M. P. Ryan, Acid resistant functionalised magnetic nanoparticles for radionuclide and heavy metal adsorption, *J. Colloid Interface Sci.*, 2022, **608**, 1728–1738.
27 E. Calì, *et al.*, Functionalised magnetic nanoparticles for uranium adsorption with ultra-high capacity and selectivity, *J. Mater. Chem. A*, 2018, **6**, 3063–3073.
28 R. Koole, *et al.*, On the Incorporation Mechanism of Hydrophobic Quantum Dots in Silica Spheres by a Reverse Microemulsion Method, *Chem. Mater.*, 2008, **20**, 2503–2512.
29 E. Calì, *Nanoparticle Technology in Radionuclide-Waste Remediation*, 2017, DOI: 10.25560/64906.
30 H. L. Ding, *et al.*, Fe_3O_4@SiO_2 Core/Shell Nanoparticles: The Silica Coating Regulations with a Single Core for Different Core Sizes and Shell Thicknesses, *Chem. Mater.*, 2012, **24**, 4572–4580.
31 R. Perez-Casero, *et al.*, Thin films of oxygen-deficient perovskite phases by pulsed-laser ablation of strontium titanate, *Phys. Rev. B:Condens. Matter Mater. Phys.*, 2007, **75**, 165317.
32 C. Destrée, F. Debuigne, L. Jeunieau and J. B. Nagy, Mechanism of formation of inorganic and organic nanoparticles from microemulsions, *Adv. Colloid Interface Sci.*, 2006, **123–126**, 353–367.
33 C. J. Bolton and A. N. Campbell, Performance of concrete structures for nuclear reprocessing plant ? review of current research and future requirements, in *Role of Concrete in Nuclear Facilities*, Thomas Telford Publishing, 2005, pp. 117–126, DOI: 10.1680/rocinf.34099.0012.
34 O. Cizer, K. V. Balen, D. V. Gemert and J. Elsen, Carbonation and hydration of mortars with calcium hydroxide and calcium silicate binders, in *Sustainable Construction Materials and Technologies*, CRC Press, 2007.
35 R. K. Abu Al-Rub, B. M. Tyson, A. Yazdanbakhsh and Z. Grasley, Mechanical Properties of Nanocomposite Cement Incorporating Surface-Treated and Untreated Carbon Nanotubes and Carbon Nanofibers, *J. Nanomech. Micromech.*, 2012, **2**, 1–6.
36 I. G. Richardson and G. W. Groves, Microstructure and microanalysis of hardened ordinary Portland cement pastes, *J. Mater. Sci.*, 1993, **28**, 265–277.
37 A. Hartmann, M. Khakhutov and J. Buhl, Hydrothermal synthesis of CSH-phases (tobermorite) under influence of Ca-formate, *Mater. Res. Bull.*, 2014, **51**, 389–396.
38 P. Sikora, *et al.*, The effects of seawater on the hydration, microstructure and strength development of Portland cement pastes incorporating colloidal silica, *Appl. Nanosci.*, 2020, **10**, 2627–2638.